ORIGINAL ARTICLE

Local Microcircuitry of PaS Shows Distinct and Common Features of Excitatory and Inhibitory Connectivity

Rosanna P. Sammons[1], Alexandra Tzilivaki[1,2,3] and
Dietmar Schmitz[1,2,3,4,5,6],

[1]Charité–Universitätsmedizin Berlin, corporate member of Freie Universität Berlin, and Humboldt-Universität zu Berlin, [2]Einstein Center for Neurosciences (ECN) Berlin, 10117 Berlin, Germany, [3]Neurocure Cluster of Excellence, Charité - Universitätsmedizin Berlin, corporate member of Freie Universität Berlin and Humboldt-Universität zu Berlin, Charitéplatz 1, 10117 Berlin, Germany, [4]German Center for Neurodegenerative Diseases (DZNE) Berlin, 10117 Berlin, Germany, [5]Bernstein Center for Computational Neuroscience (BCCN) Berlin, 10115 Berlin, Germany and [6]Max-Delbrück-Center (MDC) for Molecular Medicine, 13125 Berlin, Germany

Address correspondence to Dietmar Schmitz. Charité–Universitätsmedizin Berlin, Freie Universität Berlin, Humboldt-Universität zu Berlin, and Berlin Institute of Health, Charitéplatz 1, 10117 Berlin, Germany. Email: dietmar.schmitz@charite.de; Rosanna P. Sammons. Email: rosanna.sammons@charite.de

Abstract

The parasubiculum (PaS) is located within the parahippocampal region, where it is thought to be involved in the processing of spatial navigational information. It contains a number of functionally specialized neuron types including grid cells, head direction cells, and border cells; and provides input into layer 2 of the medial entorhinal cortex where grid cells are abundantly located. The local circuitry within the PaS remains so far undefined but may provide clues as to the emergence of spatially tuned firing properties of neurons in this region. We used simultaneous patch-clamp recordings to determine the connectivity rates between the 3 major groups of neurons found in the PaS. We find high rates of interconnectivity between the pyramidal class and interneurons, as well as features of pyramid-to-pyramid interactions indicative of a nonrandom network. The microcircuit that we uncover shares both similarities and divergences to those from other parahippocampal regions also involved in spatial navigation.

Key words: circuits, excitatory, inhibitory, PaS, spatial navigation, synaptic connectivity

Introduction

The parasubiculum (PaS) lies centrally in the parahippocampal region, neighbored medially by the presubiculum and laterally by the medial entorhinal cortex (MEC). The PaS is home to many functionally specialized neurons including grid cells, border cells, and head-direction cells (Boccara et al. 2010). Together these spatially tuned neurons are thought to underpin the brain's internal map of the environment, and thus, support navigation and spatial memory (Moser et al. 2008). The discovery of place cells (O'Keefe and Dostrovsky 1971) and grid cells (Hafting et al. 2005) in the hippocampus and MEC respectively, means much of the early focus on navigational circuitry was directed at these structures. However, the later discovery of spatially tuned neurons in other brain regions including the

presubiculum and PaS (Boccara et al. 2010), along with lesion studies from these structures showing the impairment of spatial navigation and disruption of place cells (Liu et al. 2001, 2004) has led to increased research into these brain regions. In order to understand how the wider circuitry contributes to the generation and modulation of spatially tuned signals, it is important that we also understand the local circuitry of each region. Although the local microcircuit of the presubiculum has recently been established (Peng et al. 2017), that of the PaS remains unclear.

Anatomical Connections In and Out of the PaS

One indicator of the importance of the PaS in the navigational circuit is the location of this structure within the wider parahippocampal circuitry. Anatomical tracing studies have revealed the input sources to the PaS, which include the medial septum (Unal et al. 2015; Tang et al. 2016) and the anterior thalamus (van Groen and Wyss 1990; Ding 2013). Further inputs come from the subiculum and the CA1 (van Groen and Wyss 1990; Ding 2013; O'Reilly et al. 2013), the presubiculum (Köhler 1986; O'Reilly et al. 2013), postrhinal cortex (Agster and Burwell 2013) and the basolateral amygdala (van Groen and Wyss 1990). Thus, the PaS receives input from a number of regions known to be involved in navigation and memory. The medial septum is known to be a key pacemaker structure involved in orchestrating theta oscillations in the hippocampus (Petsche et al. 1962; Mitchell et al. 1982; Buzsáki 2002). The anterior thalamus is the region with the greatest abundance of head-direction cells (Taube 2007; Winter et al. 2015) and neighboring input structure, the presubiculum, is also home to many head-direction cells (Taube et al. 1990; Boccara et al. 2010). On the output side, one of the major downstream targets of the PaS is layer 2 of the MEC (Köhler 1986; Caballero-Bleda and Witter 1993; Agster and Burwell 2013). Specifically, the calbindin-patches have been proposed to be the target of parasubicular afferents, although direct functional evidence for this is still lacking (Tang et al. 2016). Further projections from the PaS have also been shown in the lateral entorhinal cortex, (Agster and Burwell 2013), CA1, subiculum, and presubiculum (van Groen and Wyss 1990). The PaS also sends contralateral projections to the presubiculum, PaS and MEC (van Groen and Wyss 1990). The projection to layer 2 of the MEC is particularly relevant to the navigational circuitry, since this is where the highest abundance of grid cells is found (Boccara et al. 2010). Thus, the PaS is well positioned to influence grid cell firing in the MEC.

Cytoarchitecture of the PaS

Although neighboring structures to the PaS both show spatially tuned signals, the cellular composition of these brain regions appears to be quite different. Immunohistochemistry work has helped to uncover the cellular composition of the PaS and distinguish it from the presubiculum and MEC. The PaS can be identified by its strong wolframin (WFS1) expression (Ding 2013; Ramsden et al. 2015; Ray et al. 2017). This transmembrane protein is completely absent in the presubiculum, delineating a clear border between these 2 structures (Luuk et al. 2008). While WFS1 is also present in layer 2 of the MEC, a number of key distinctions can be made between the PaS and the MEC. The MEC is a classically 6-layered cortical structure (Witter et al. 2017). Meanwhile, the layering of the PaS remains ambiguous, with some studies referring to it as a 6-layered structure (Funahashi and Stewart 1998; Glasgow and Chapman 2007;

Boccara et al. 2010), and others arguing that it consists only of 3 layers (Mulders et al. 1997; Burgalossi et al. 2011; Tang et al. 2016). Regardless of the number of layers, some key differences have been established. Layer 2 of the MEC is home to 2 classes of principal neurons: pyramidal neurons expressing WFS1 and calbindin (Kitamura et al. 2014), and stellate cells expressing reelin (Varga et al. 2010; Ray and Brecht 2016). Although some studies have also described stellate and pyramidal neurons in the PaS (Funahashi and Stewart 1997, 1998) their distinction in this region is less clear and specific markers for the 2 cell types are lacking. In the PaS, reelin is predominantly expressed in inhibitory neurons, whereas calbindin is expressed exclusively in inhibitory neurons (Sammons et al. 2019). Thus, the colocalization of calbindin and WFS1 can be used to distinguish the border between the PaS and the MEC. Further differences in the cytoarchitecture of these 2 regions come from cytochrome oxidase labeling, which shows a pattern of small patch-like labeling in layer 2 of the MEC, whereas the PaS appears to be labeled by few larger patches (Burgalossi et al. 2011). Detailed single cell labeling of cells from these large patches shows axonal arborizations extending several hundred micrometers through neighboring large patches and into the MEC, providing further evidence of the connectivity from the PaS to the MEC.

A small transition zone between the PaS and MEC has now been described by several groups (Fujimaru and Kosaka 1996; Ray et al. 2017), which may correspond to the previously described "parasubiculum A" subregion (Blackstad 1956; Slomianka and Geneser 1991). This transition region also shows colocalization between WFS1 and calbindin, suggesting it may be more similar to the MEC than the PaS. Furthermore, the primary dendrites of neurons in this region tend to project toward layer 1 of the MEC rather than into the PaS, indicating that they are the recipient of inputs targeted to the superficial MEC, and thus, are part of this structure (Sammons et al. 2019).

Functional Properties of PaS Neurons

Several functional properties of parasubicular neurons have been described. Neurons in the PaS exhibit strong theta rhythmicity, (Burgalossi et al. 2011; Ebbesen et al. 2016; Tang et al. 2016), likely in part due to the strong connection from the medial septum. Additionally, in vitro work has also shown that parasubicular neurons exhibit conductances capable of producing intrinsic membrane potential oscillations in the theta range, which may also contribute to the strong theta activity seen in this region (Glasgow and Chapman 2008). A large proportion of neurons in the PaS show head-direction selectivity (Tang et al. 2016) and a population of neurons that combine theta-modulation and spatial location coding, known as theta-modulated place-by-direction cells have also been described (Cacucci et al. 2004). Similar theta-modulated head-direction cells have also been described in the anterior thalamus, and thus, may be the source of such signals in the PaS (Cacucci et al. 2004; Tsanov et al. 2011). Given the functional evidence of spatially modulated signals in the PaS and the anatomical evidence placing this region upstream of the MEC, the PaS is well positioned to influence the spatial tuning of neurons in the MEC and play a key role in the navigational circuitry.

Computational models have been developed to understand how grid-like patterns of activity and other spatially—modulated firing patterns may come about. Models fall largely into 2 classes, the oscillatory interference models (Burgess et al. 2007; Hasselmo et al. 2007; Blair et al. 2008), and continuous attractor network models (Fuhs and Touretzky

2006; McNaughton et al. 2006; Burak and Fiete 2009), whereas hybrid models seek to combine features from both classes (Hasselmo and Brandon 2012; Schmidt-Hieber and Häusser 2013; Bush and Burgess 2014). Despite these models, the exact mechanisms underlying spatially tuned firing properties are still unresolved. Mapping out the fine details of the microcircuitry in which these cells sit is an essential step to further develop our understanding. Experimental work has provided key constraints for these models of grid cell and head-direction activity (Couey et al. 2013; Buetfering et al. 2014; Fuchs et al. 2016; Peng et al. 2017; Winterer et al. 2017). However, the local circuitry in the PaS has not yet been resolved. We take a similar approach to previous connectivity studies and use the multicell patch clamp technique to uncover the local connectivity within the PaS.

Materials and Methods

A full list of resources used can be found in Supplementary Table 1. (Location for the link to the Supplementary Table 1 Resources).

Animals

All animal maintenance and experiments were performed in accordance with institutional guidelines, guidelines of the local state government (Berlin state government, T0100/03; O0413/12), and the European Union Council Directive 2010/63/EU.

Electrophysiology

Slice Preparation
Slices were prepared from adult (postnatal day 50 and over) C57/Bl6n mice of both sexes. A small number of slices were taken from transgenic animals being used for additional projects (C57/Bl6n: $N = 79$ animals, $n = 127$ slices; VGAT-YFP: $N = 11$, $n = 18$; ChAT-Cre: $N = 11$, $n = 15$; PV-Cre: $N = 3$, $n = 5$; WFS1-Cre: $N = 3$, $n = 4$). Animals were anesthetized under isoflurane and decapitated. Brains were removed and transferred to an ice-cold, sucrose-based dissection artificial cerebrospinal fluid containing, in mM: 87 NaCl, 26 NaHCO$_3$, 50 sucrose, 10 glucose, 2.5 KCl, 1.25 NaH$_2$PO$_4$, 0.5 CaCl$_2$, 3 MgCl$_2$, and saturated with 95% O$_2$ and 5% CO$_2$. Horizontal slices, 400 μm thick, were cut using a vibrating microtome slicer (VT1200S, Leica Biosystems), throughout the dorsoventral axis of the PaS. Once cut, slices were transferred to an interface chamber, which was continuously perfused with ACSF containing, in mM: 119 NaCl, 26 NaHCO$_3$, 10 glucose, 2.5 KCl, 1.3 MgCl$_2$, 1 NaH$_2$PO$_4$, 2.5 CaCl$_2$, saturated with 95% O$_2$ and 5% CO$_2$ and maintained at 32–34°C. Slices were allowed to recover for at least 1 h before being transferred to a recording chamber.

Whole-cell Recordings
Recordings were performed in a submerged chamber, kept at 32–34°C, and perfused with the same ACSF as used for interface storage. Somatic whole-cell recordings were performed using glass pipettes pulled from borosilicate glass capillaries with a resistance of 3–6 MΩ. Pipettes were pulled using a horizontal DMZ Universal Puller (Zeiss, Germany) and filled with an internal solution containing, in mM: 120 K-Gluconate, 10 HEPES, 10 KCl, 5 EGTA, 2 MgSO4.7H20, 3 MgATP, 3 NaGTP, 5 Phosphocreatine Na. Internal solution also contained 0.2% Biocytin, to allow for later identification of recorded neurons. Cells in the PaS were visually identified using infrared differential interference contrast microscopy through a digital camera (XM10-IR, Olympus).

Recordings were performed using Multiclamp 700A/B amplifiers (Molecular Devices). Signals were filtered at 10 kHz and sampled at 20 kHz, digitized using Digidata 1550 and recorded in pClamp10 (Molecular Devices, United States of America). Series resistance was calculated from the current deflection to a −4 mV injection applied in voltage clamp. Pipette capacitance neutralization and bridge balance were applied and adjusted as appropriate. Liquid junction potential was not corrected for. Either 4 or 8 electrodes were used to target up to 8 potential cells for recording. All electrodes to be used were first brought to just above the surface of the slices, over the center of the PaS. Electrodes were then each sequentially used to target a cell and successfully patched cells were left in the whole-cell configuration in voltage clamp, while subsequent cells were targeted. Once all electrodes in use had been placed, recording of successfully patched cells began. Neurons were switched to the current clamp configuration and characterized by injecting increasing steps of negative and positive current. Current injections were applied for 1 s, in increasing steps of 40 pA. The voltage responses of neurons to these current injections were used to calculate intrinsic properties and action potential (AP) parameters. Connectivity was screened by stimulating each cell in turn to produce 4 APs (1000–4000 pA for 1–2 ms) at 20 Hz. The connectivity screen was carried out in current clamp with cells at resting membrane potential, and while injecting current to hold cells at −50 mV to elucidate any inhibitory postsynaptic potentials (IPSPs). Connectivity screens consisted of 30–50 sweeps. An average trace was created by first passing each sweep through a quality check. Recordings with fewer than 20 sweeps remaining following this check were discarded. Individual sweeps were discarded if the membrane potential fluctuated by more than 10% from the start to the end of the sweep, or if it deviated by more than 10% from the original membrane potential value. All remaining sweeps were then averaged and this average examined for the presence of postsynaptic potentials that closely aligned with the presynaptic APs. If a connection was ambiguous from the average trace, sweeps were examined on an individual basis to determine if a postsynaptic response was visible in multiple sweeps or if a single individual, spontaneous postsynaptic potential was heavily influencing the average trace. All connection parameters were measured using the average trace. Onset latency was calculated as the time between presynaptic AP peak and the foot of postsynaptic potential. The foot of the postsynaptic potential was defined as the intersection between the baseline of the postsynaptic cell and the 20–80% slope of the response. Rise time (10–90%) and halfwidth of postsynaptic potentials were measured in Stimfit (Guzman et al. 2014). Cells were recorded within 300 μm of each other. At the end of recording, an image of the slice and electrode placement was taken through a 4× objective to aid with reidentification of the recorded neurons.

Imaging

Immunohistochemistry
Following recording, slices were fixed in 4% paraformaldehyde (PFA) overnight. Sections were then washed 3 times (5 min each) in phosphate-buffered saline (PBS) before being incubated in a blocking solution composed of 5% normal goat serum (NGS, Biozol), 1% Triton-X (Sigma) and PBS, for 3 h at room temperature with gentle agitation. Subsequently, slices were incubated with primary antibody for 72 h at 4°C. All slices were labeled with anti-WFS1 (1:1000) to aid with demarcation of the PaS, as well as to label

potential excitatory neurons. Since non-fast-spiking interneurons are harder to differentiate from pyramidal neurons, the majority of slices were labeled additionally with an anti-Reelin antibody (1:1000). However, in order to provide some true positive parvalbumin (PV) neurons for our classification, some slices with suspected fast-spiking interneurons were labeled with anti-PV, instead of anti-Reelin (1:1000). Slices from vesicular gamma-Aminobutyric acid (GABA) transporter- yellow fluorescent protein (VGAT-YFP) animals were additionally labeled with anti-YFP (1:500). Primary antibodies were diluted in a blocking solution composed of 2.5% NGS, 1% Triton-X, and PBS. To label the biocytin, a conjugated streptavidin marker was used (conjugated to either AF 488 or AF 647, concentration 1:500). Following primary incubation, slices were washed 3 times in PBS (20 min each) and incubated in secondary antibodies for 3 h at room temperature. Secondary antibodies were applied at 1:500, diluted in PBS (Life Technologies). In most cases, secondary antibodies used were anti-rabbit 647 and anti-mouse 555. In the case where anti-YFP was also used for primary incubation secondary antibodies used were antirabbit 405, antichicken 488, and antimouse 555. Finally, slices were washed 4 times (15 min) before being mounted on glass slides in mounting medium (Mowiol).

Confocal Microscopy
Slices were imaged on a Leica TCS SP5 confocal microscope (Leica Microsystems), using 405 nm (diode), 488 nm (Argon), 568 nm (solid state), and 633 nm (Helium, Neon) laser lines. Images were taken through a 20× immersion (0.7 N.A., Leica, pixel size 0.72 µm) and a 63× (1.4 N.A., Leica, pixel size 0.23 µm) objective to provide an overview image and close up of cell somata respectively. Images were acquired at 1024 x 1024 pixels, with a z-step of 2 µm (20×) or 0.5 µm (63×). Images were analyzed in Fiji (Schindelin et al. 2012). Close-up images of cell somata were used to determine any post hoc immunolabeling and overview images were used to measure the distance from cell soma to the pia, as well as for matching up cells with their respective recording headstages and confirming that cells were located within the PaS. Cells were confirmed to be within the PaS by examining WFS1 labeling which provides a clear border with the presubiculum on the medial side. On the lateral side of the PaS, the border with the MEC is less well defined since WFS1 is present also in layer 2 of the MEC. A transitional zone, the medial-most MEC has been described between these 2 brain regions (Fujimaru and Kosaka 1996; Ray et al. 2017), which also expresses WFS1 throughout. Cells were assigned to this region and excluded from the PaS based on the projection angle of their dendrites as previously described (Sammons et al. 2019). Cells whose dendrites projected in the direction of the superficial MEC (i.e., in a lateral direction) were excluded, whereas cells whose dendrites projected in a medial direction, and therefore, toward the center of the PaS were assigned to the PaS.

Quantification and Statistical Analysis

Analysis of Electrophysiological Properties
Electrophysiological properties were extracted using custom-written python scripts. The following properties were used as input parameters for classification: resting membrane potential (Vm), input resistance, AP threshold, AP height, afterhyperpolarization (AHP), mAHP, AP1-AP2 interval, AP9-AP10 interval, adaptation, latency, maximum and minimum dV/dt, dV/dt ratio, rheobase, sag ratio minimum interspike interval, membrane

capacitance, and membrane time constant. Vm was taken as the mean across all sweeps of the baseline before current injection. Input resistance was calculated from the voltage deflection in response to a −80 pA current pulse. Sag ratio was calculated from a −200 pA current pulse, by dividing the voltage difference between baseline and the steady state by the difference between baseline and the minimal voltage reach within the first 100 ms after current injection onset. Rheobase was taken as the current step first seen to elicit an AP. AP threshold was taken as the membrane potential at the point where dV/dt reached 5% of the maximal dV/dt. AP height was calculated as the difference between threshold and the peak amplitude of the first AP. Latency was defined as the time between current injection onset and the initial AP in the first sweep where 10 APs were seen. AP half-width was calculated from the first AP, using the time between the half-height of the upward and downward slopes. Interspike intervals were calculated as the time difference in onset of subsequent APs, from sweeps where at least 10 APs were elicited. Adaptation was calculated by dividing the intervals between the ninth and tenth APs and the second and third APs. If a cell did not produce 10 APs, the sweep with the maximal number of APs was used. Minimal interspike interval was taken as the minimum interval between any 2 consecutive APs. Maximum firing frequency was taken as the maximal number of APs produced by current injection. AHP was calculated as the difference between AP threshold and the minimum voltage seen within 2 ms of AP peak. Medium AHP was defined as the difference between threshold and the minimum voltage seen within 200 ms of current injection offset. Membrane capacitance and membrane time constant were calculated from the voltage response to a −160 pA current injection.

Cell Classification
Cells were classified into 3 classes based on previous work (Sammons et al. 2019) using a combination of immunohistochemistry and electrophysiological parameters. We used WFS1, PV, and reelin to approximate the 3 major cell classes, namely pyramidal neurons, fast-spiking interneurons, and non-fast-spiking interneurons, respectively. Staining information was available for 272 out of 514 cells. For cells without immunolabeling we took a machine learning (ML) approach to classify them to one of the 3 classes, based on their intrinsic and firing properties. In a few cases, not all electrophysiological parameters were available for a cell. In this instance, if staining information was available the mean value of missing parameter from all other cells with the same immunolabel was assigned. If staining information was not available the "KNNImputer" function (sklearn) was used to assign the missing value. Given that our data belong to a multiclass and imbalanced case (236 WFS1 positive, 28 reelin positive, and 8 PV positive neurons), we aimed to select the most accurate classification algorithm for our dataset by testing several models including Complement Naïve Bayes, Logistic Regression, k-Nearest Neighbors Classifier, Random Forest Classifier (RFC), Support Vector Classifier, and Multilayer Perceptron (MLP)—Artificial Neural Network. For each algorithm, we used the subpopulation of neurons with known staining ($n = 272$) to train and test the output performance of the classifier. The "GridsearchCV" function (Sklearn) was used to identify the best parameters for each model and class weights were calculated and inserted to models where applicable. We used stratification and cross validation to select the 2 highest performing models (RFC and MLP) and further tested their performance

Table 1 Performance scores for classification models

	Accuracy	Balanced Accuracy	Precision	Recall	F1 Score	ROC AUC score
RF	0.94/(0.007)	0.87/(0.04)	0.916/(0.06)	0.878/(0.04)	0.88/(0.029)	0.97/(0.029)
MLP	0.948/(0.02)	0.88/(0.075)	0.93/(0.025)	0.88/(0.07)	0.89/(0.05)	0.96/(0.036)

Note: Mean and SD range for performance metrics of random forest (RF) and MLP classification models.

using multiple metrics (Table 1). To produce the final prediction classes for cells without immunolabeling, we ran the 2 top-performing algorithms multiple times and took the mode class result. The resulting predictions agreed in 89% of cells across the 2 algorithms. Therefore, since both algorithms performed equally well we excluded the minority of cells where the final prediction disagreed from our final dataset ($n = 27/242$ cells).

Statistics

Statistics were carried out in python using "scipy" and "statsmodels" packages. Data were assessed for a normal distribution using the Shapiro–Wilk test. Where the null hypothesis was rejected, median and interquartile range (IQR) are reported and the Mann–Whitney U test was applied. When the null-hypothesis could not be rejected, mean ± standard deviation (SD) are reported and Student's t-tests were performed. To test whether intersomatic distance had an effect on connectivity rates, the ordinal association test (Cochran-Armitage trend test) was performed. To determine if projection direction had an effect on connection probability, a projection distance was calculated for each pair of tested projections by subtracting the minimal distance to pia measure of the postsynaptic cell from the minimal distance to pia of the presynaptic cell. Tested connections were then assigned as either deep-to-superficial or superficial-to-deep depending on the sign of this sum. Projection distances between ±10 μm were excluded from this analysis. A Fisher's exact test was used to compare connection probabilities across the 2 possible directions. To test whether reciprocal connections were observed more often than expected a simple binomial test was performed, with the hypothesized probability set to the product of the 2 independent connectivity probabilities. The alpha level for rejecting the null hypothesis was set to 0.05 for all tests.

Data and Software Availability

Code Availability

Code used for the analysis of electrophysiology and cell classification can be found on Github under https://github.com/rosa nnaps/PaS-analysis.git

Results

Connectivity Scheme between the Major Cell Classes in the PaS

We recorded simultaneously from up to 6 neurons (1 sextuple, 7 quintuple, 13 quadruple, 47 triple, and 101 double recordings) in a whole-cell patch-clamp configuration in the PaS, to elucidate the microcircuitry within this region (Fig. 1A). The PaS was identified in acute slices based on the size and organization of cell somata; somata in the PaS are larger than in the pre-subiculum. Meanwhile, the lack of easily identifiable layering distinguishes the PaS from the MEC in mouse. The location of all

cells was confirmed post hoc by examining biocytin and WFS1 labeling (Fig. 1B; see Materials and Methods). Previously, we have shown that neurons in the PaS can be broadly classified into 3 groups: fast-spiking putatively PV-expressing interneurons, a broad class of non-fast-spiking interneurons often expressing reelin, and a large class of pyramidal neurons typically expressing WFS1 (Sammons et al. 2019). We used these groups to classify our recorded neurons, using a combination of immunolabeling and electrophysiological properties. In total, we recorded from 514 neurons in the PaS and were able to reliably detect a positive immunomarker in 272 of these cells (236 WFS1-positive, 28 reelin-positive, 8 PV-positive; Fig. 1C). To classify the remainder of cells with no immunolabeling information, we applied a ML approach, where the electrophysiological features of cells with known labeling were used to train classifiers in order to assign nonlabeled cells to 1 of our 3 cell classes based on their electrophysiological properties (see Materials and Methods, Table 1; for electrophysiological properties of the 3 cell classes see Table 2). A small fraction of cells ($n = 27$) was excluded due to ambiguous classification. Thus, we were able to establish a connectivity scheme between these main subgroups of neurons in the PaS (Fig. 1D–E). For all connections where the presynaptic cell was classified in 1 of the 2 interneuron classes, IPSPs were seen in the postsynaptic cell leading us to believe that our classification could robustly separate excitatory and inhibitory neurons. Pyramidal neurons form the biggest cell class in the PaS. We observed a connectivity rate of 4% between cells of this class (25/622 tested connections; Fig 1D). Reciprocal connections were observed between 3 separate pairs of pyramidal neurons (3/311 pairs tested, 0.96%). This observed frequency is higher than expected based on a 4% connectivity rate (expected likelihood of reciprocal connectivity: 4% × 4% = 0.16%, $P = 0.014$, binomial test), suggesting a nonrandom organization of connectivity between pyramidal neurons in the PaS.

We found connections between both classes of inhibitory neurons and the pyramidal class of cells. Specifically, non-fast-spiking interneurons connected onto pyramidal neurons at a rate of 13% (5/38 tested connections), whereas fast-spiking neurons showed a 44% connectivity rate onto pyramidal neurons (17/39 tested connections). In the opposite direction, pyramidal neurons contacted non-fast-spiking neurons at a relatively low rate (2.6%, 1/38 test connections, unidirectional), but contacted fast-spiking neurons at a rate of 23% (9/39 tested connections). Between pyramidal and fast-spiking neurons 5 reciprocally connected pairs were found (5/39 pairs, 12.8%). Given the individual connectivity rates between these 2 cell classes the number of reciprocal pairs found was not different from expected (expected likelihood of reciprocal connectivity: 44% × 23% = 10.1%, $P = 0.591$, binomial test).

Pyramid to Pyramid Connections in the PaS

The pyramidal class of neurons consisted of WFS1-positive immunolabeled neurons, as well as nonlabeled neurons with comparable electrophysiological profiles (Fig. 2A1). Connections
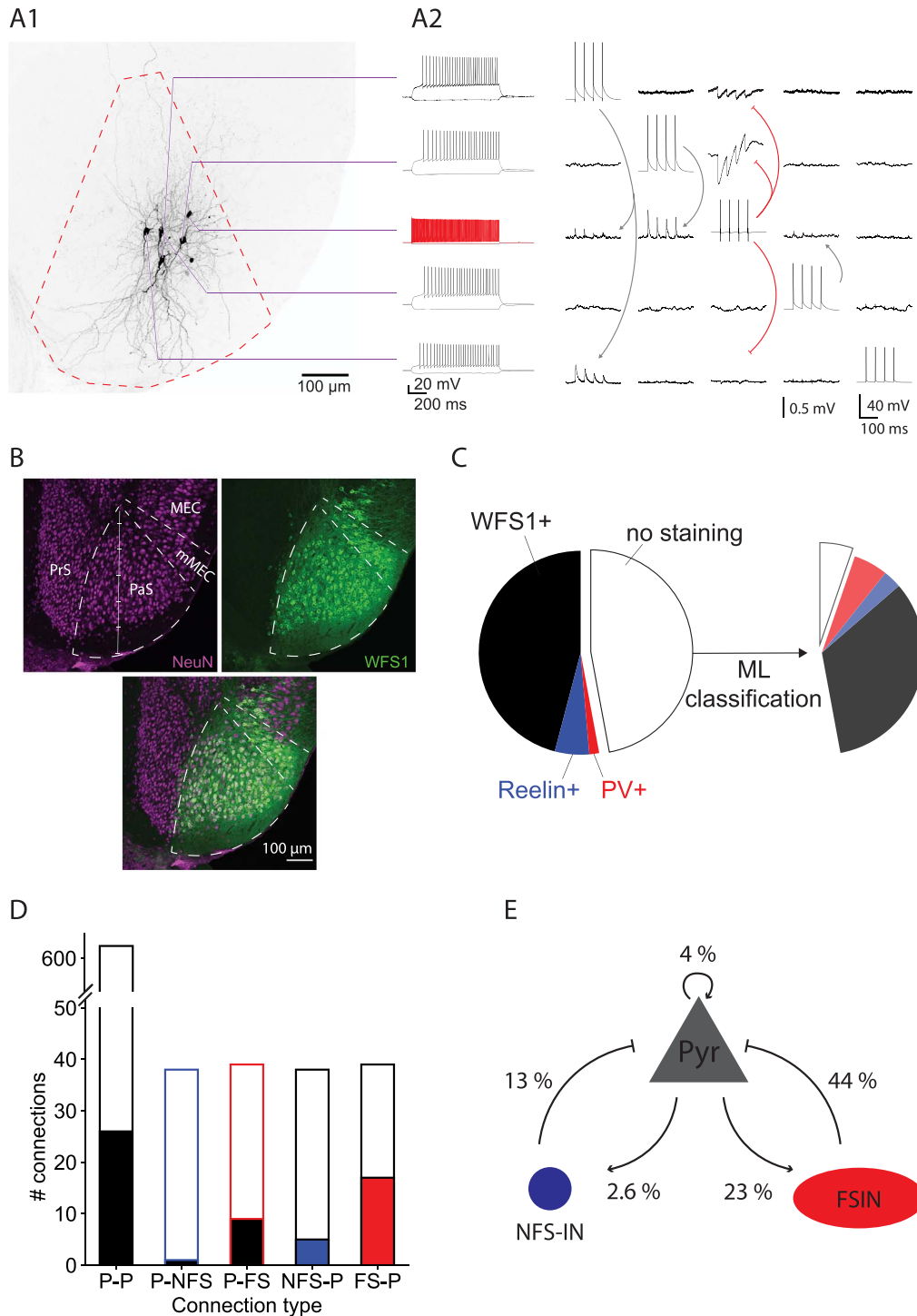
Figure 1. Connectivity rates across the 3 major cell classes in the PaS. (A1) Biocytin labeling of a cluster of 5 recorded neurons. (A2) Left, firing profile of the cells shown in A1. Right, connectivity screen. Each cell is consecutively stimulated to fire 4 APs, whereas the postsynaptic cell membrane potential is monitored. Postsynaptic traces displayed are an average of 50 sweeps. 40 mV scalebar refers to presynaptic AP traces, 0.5 mV bar refers to postsynaptic response traces. (B) Immunolabeling of NeuN (magenta) and WFS1 (green) to demarcate the PaS. (C) Proportion of immunolabeled neurons from the whole dataset, and the proportion of nonlabeled neurons assigned to each cell class following ML (ML) classification. The nonfilled portion after classification represents cells with ambiguous assignment, which were subsequently excluded from the dataset. (D) Numbers of tested (open bars) and found connections (filled bars) between the different cell classes. (E) Summary of connectivity rates between pyramidal neurons and the 2 subgroups of interneurons in the PaS.

Table 2 Electrophysiological properties of PaS cell types

	Pyramid, $n = 408$	Non-fast-spiking interneuron, $n = 43$	Fast-spiking interneuron, $n = 36$
Vm (mV)	−66.3 (−71.4—−60.2)	−65 (−70.5—−60.6)	−65.8 (−72—−62.3)
Input resistance (MΩ)	106.3 (80.1–133.9)	211.4 (148.2–271.9)	55.7 (48.3–73.1)
Sag Ratio	0.89 (0.85–0.92)	0.9 (0.85–0.93)	0.92 (0.89–0.95)
Membrane time constant (ms)	9.6 (7.7–11.8)	6.8 (5.1–10.3)	4 (3.4–4.4)
Membrane capacitance (pF)	106.7 (85.2–129.4)	47.7 (30.6–56.6)	74.8 (59.8–87.9)
Rheobase (pA)	160 (120–200)	80 (40–120)	400 (280–500)
AP threshold (mV)	−33.3 (−35.7—−31.4)	−33.8 (−36.6—−31.1)	−32.6 (−36.5—−30.3)
AP half-width (ms)	0.69 (0.61–0.79)	0.68 (0.50–0.83)	0.24 (0.21–0.27)
AP height (mV)	65.9 (58.9–71.6)	48.5 (44.1–59.3)	48.7 (45–55.4)
Onset latency (ms)	288.7 (176.7–498)	83.8 (41–145.9)	34.1 (8.4–319.9)
Max dV/dt (V.s^{-1})	254 (195–316)	179 (135–256)	354 (286–417)
Min dV/dt (V.s^{-1})	−106 (−125—−86)	−96 (−134—−66)	−282 (−346—−220)
dV/dt ratio	2.4 (2.0–2.8)	1.9 (1.6–2.2)	1.2 (1.1–1.3)
AP1-AP2 int. (ms)	66.3 (52.7–76.8)	29 (18.5–40.4)	9.5 (7.6–17.3)
AP9-AP10 int. (ms)	58 (47.4–72.6)	37.1 (27.2–56)	10.4 (8.1–17.2)
Adaptation index	0.94 (0.82–1.12)	1.13 (0.82–1.44)	1.02 (0.75–1.21)
Min. ISI (ms)	10.6 (7.8–16.4)	4.2 (3.6–5)	3.9 (3–5.4)
Max. firing freq (Hz)	51 (37–65)	91 (61–119)	229 (160–302)
AHP (mV)	15.8 (13.3–18.3)	18 (14.9–21.4)	25.7 (23.4–27.6)
mAHP (mV)	2.3 (0.9–3.5)	2 (0.7–4.4)	1.7 (1.1–2.6)

between this class of neurons produced excitatory postsynaptic potentials (EPSPs) in the postsynaptic cell (Fig. 2A2) confirming the excitatory nature of WFS1 neurons. The strength of these connections followed a log-normal distribution, with many small EPSPs and a small number of large EPSPs (median EPSP amplitude 0.43 mV, 0.17–0.89 IQR; Fig. 2B). EPSPs between pyramidal neurons had a median latency of 1.55 ms, 1.2–2.65 IQR, mean halfwidth of 15.4 ± 8.6 ms and a mean rise time of 2.1 ± 1.0 ms (Fig. 2C–E). In contrast to other brain regions, we did not find bidirectional connections to be stronger than unidirectional connections in the PaS (Table 3) (Song et al. 2005; Cossell et al. 2015; Peng et al. 2017). However, bidirectional connections did have significantly smaller halfwidths and rise times than unidirectional connections (Table 3).

We next aimed to determine if there was any spatial influence of connectivity rates between pyramidal neurons. We recorded from pyramidal neurons across a range of depths across the superficial-deep axis (Fig. 2F). The majority of recorded neurons were located between 100 and 300 μm from the pial surface, corresponding to where these cells represent the majority of neurons in the PaS (Sammons et al. 2019). We first looked at the absolute intersomatic distance between recording pairs (Fig. 2G). The median intersomatic distance between recorded pyramidal neuron pairs was 87 μm, 66–112 IQR. The connectivity rate did not significantly differ across the range of intersomatic distances tested. Another spatial aspect that could influence connectivity is laminar organization. The laminar structure of the PaS in rodents is ambiguous; however, (Mulders et al. 1997; Tang et al. 2016). Thus, we used a minimal distance to pia measure to examine connectivity along the superficial-to-deep axis. For each pair of recorded neurons, the minimum distance to pia measure of the postsynaptic cell was subtracted from that of the presynaptic cell, such that connections projecting from a deep to a more superficial cell would have a positive projection distance and connections from a superficial to a deeper cell would have a negative projection distance (Fig. 2H, inset). Connectivity occurred in both

directions and was not significantly more likely to occur in one direction more than the other (Fig. 2H). Finally, to determine if a particular region may be more enriched in connectivity than another, we grouped neurons based on the mean distance-to-pia measure of pre- and post-synaptic partners (Fig. 2I). Although all connections were observed within 300 μm of the pia, connectivity rates were not significantly different across the binned distances measured. Similar connectivity rates across groups were also seen when only selecting pairs of neurons found in the same distance-to-pia interval (Fig. S1).

Inhibition onto Pyramidal Neurons in the PaS

Inhibitory connections were observed from both non-fast-spiking and fast-spiking interneurons onto pyramidal neurons in the PaS (Fig 3A–B). The amplitudes of IPSPs from non-fast-spiking neurons and fast-spiking neurons were not significantly different from one another (Fig. 3C; median IPSP non-fast-spiking to pyramid: −0.29 mV, −0.38 to −0.21 IQR, median IPSP fast-spiking to pyramid: −0.32 mV, −0.71–0.23 IQR; $P = 0.265$, Mann–Whitney U). In contrast, the latency of IPSPs from fast-spiking interneurons was significantly shorter than IPSPs from non-fast-spiking neurons onto pyramidal neurons (Fig. 3D; median IPSP latency: non-fast-spiking to pyramid 0.85 ms, 0.85–1.3 IQR, fast-spiking to pyramid 0.75 ms, 0.6–0.8 IQR; $P = 0.011$, Mann–Whitney U). The rise time of IPSPs from fast-spiking neurons was also significantly shorter than IPSPs from non-fast-spiking neurons (Fig. 3E; median IPSP rise time: non-fast-spiking to pyramidal neurons 8.4 ms, 5.7–9.2 IQR, fast-spiking to pyramidal neurons 1.8 ms, 1.3–2.5 IQR; $P = 0.009$, Mann–Whitney U). The halfwidths of IPSPs from the 2 classes of interneurons onto pyramidal neurons did significantly differ (Fig. 3F; mean IPSP halfwidth: non-fast-spiking to pyramidal neurons 32.4 ± 16.9 ms, fast-spiking to pyramidal neurons 21.2 ± 13.8 ms; $P = 0.146$, Student's t-test). No significant differences were seen between uni- and bidirectional connections from fast-spiking interneurons onto pyramidal neurons (Table 3).
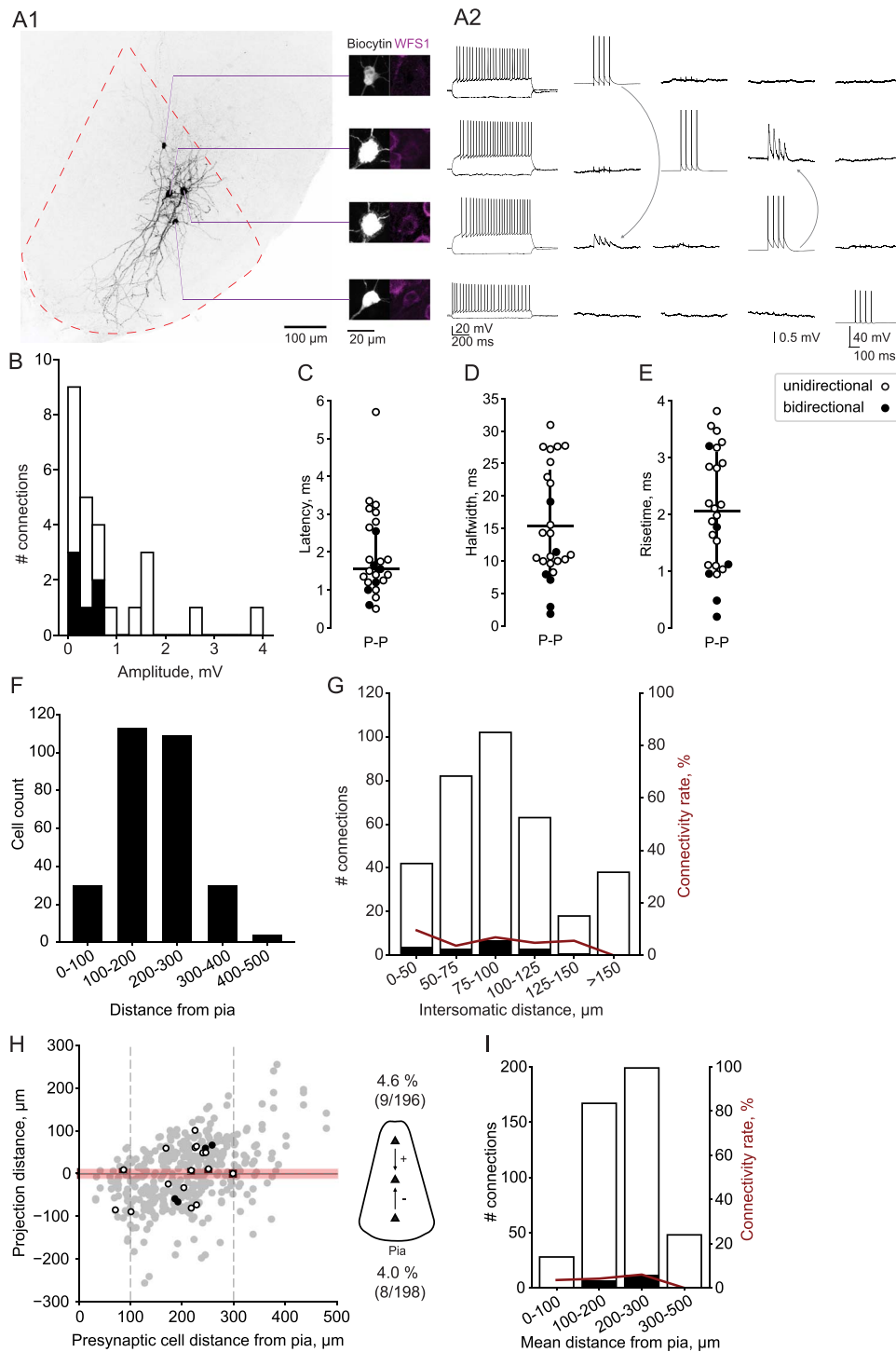
Figure 2. Pyramid to pyramid connections. (A1) Biocytin labeling of 4 simultaneously recorded pyramidal neurons in the PaS. Right, close of up somata and WFS1 labeling. In the top cell, WFS1 labeling was not detected but the cell was classified as a pyramidal neuron based on electrophysiological properties. (A2) Left, firing profiles and right, connectivity screen between 4 cells shown in A1. Postsynaptic traces are an average of 50 sweeps. (B) Histogram of EPSP amplitudes for pyramid-to-pyramid connections. $P = 0.548$, Shapiro–Wilk test on log-transformed values. Open bars represent unidirectional connections and filled bars, bidirectional connections. (C) Latency times of EPSPs for pyramid-to-pyramid connections. (D) Halfwidth of EPSPs in pyramid-to-pyramid connections. (E) Rise time of EPSPs in pyramidal connections. (F) Distribution of cells recorded from different depths with respect to the pia. (G) Number of tested (open bars) and found (filled bars) connections at different intersomatic distances. Red line represents the connectivity rate in each bin. No distance-dependence in connection probability was seen using the ordinal association test ($P = 0.242$). (H) Laminar directional dependence of connectivity with respect to presynaptic cell depth. Gray points indicate tested connections with no connectivity, black points indicate found connections (filled points correspond to bidirectional connections). Shaded red area indicates ±10 µm region discounted from statistical analysis for directional dependence. Right, schematic summarizes calculation method such that a positive value indicates deep-to-superficial connection and a negative value indicates superficial-to-deep connection. No directional-dependence was seen in connection probability using Fisher's exact test to compare connection probability from deep-to-superficial cells versus superficial-to-deep cells ($P = 0.810$). (I) Number of tested (open bars) and found (filled bars) connections, and connection rate (red line) at different mean distances from the pia; $P = 0.485$, nominal association test.

Table 3 Synaptic properties of uni and bidirectional connections

Connection type		Amplitude, mV	P value	Latency, ms	P value	Halfwidth, ms	P value	Rise time, ms	P value
Pyr-Pyr	Unidirectional, $n = 19$	0.47 (0.18–1.46)	0.107	1.8 (1.3–2.9)	0.107	14.3, (10.3–26.2)	0.009	2.2 (1.6–3.0)	0.026
	Bidirectional, $n = 6$	0.23 (0.16–0.49)		1.4 (1.1–1.6)		7.5, (3.9–10.5)		1.0 (0.6–1.6)	
Pyr-FS	Unidirectional, $n = 5$	0.30 (0.22–2.36)	0.451	1.0 (0.7–1.2)	0.450	9.6, (5.0–14.2)	0.270	0.9 (0.5–1.3)	0.451
	Bidirectional, $n = 4$	0.25 (0.19–0.66)		0.8 (0.8–1.0)		6.0, (3.4–6.4)		1.0 (1.0–1.1)	
FS-Pyr	Unidirectional, $n = 12$	−0.31 (−0.66—−0.21)	0.318	0.7 (0.6–0.8)	0.259	17.5 (6.5–29.9)	0.318	2.0 (1.2–2.5)	0.479
	Bidirectional, $n = 5$	−0.42 (−0.71—−0.27)		0.7 (0.6–0.9)		24.3 (24.3–29.2)		1.8 (1.6–1.8)	

Median and interquartile range for connection parameters in uni- and bidirectional connections of different synaptic pairings. P values are calculated from Mann–Whitney U test.

Non-fast-spiking interneurons were recorded up to 400 μm from the pia (Fig. 4A). Connectivity rates did not significantly differ across the tested intersomatic distance range for either class of interneuron onto pyramidal neurons (Fig. 4B). Furthermore, we found no directional influence on connectivity rates from non-fast-spiking interneurons onto pyramidal neurons (Fig. 4C). Fast-spiking interneurons were recorded between 100 and 400 μm from the pia (Fig. 4D), in line with previous work showing their absence from very superficial regions (Sammons et al. 2019). Connectivity rates were not significantly influenced by intersomatic distance between fast-spiking and pyramidal neurons (Fig. 4E). Moreover, connectivity rates did not statistically significantly differ according to projection direction, and connections were seen across the full range of depths of the presynaptic fast-spiking interneurons (Fig. 4F).

Pyramid to Interneuron Connections

We observed only a single connection between pyramidal neurons and non-fast-spiking interneurons. In contrast, pyramidal neurons frequently contacted fast-spiking interneurons. Similar to pyramid–pyramid connections, the strengths of pyramidal neurons to fast-spiking connections also followed a log-normal distribution (Fig. 5B). The median latency of EPSPs was 0.8 ms, 0.8–1.2 IQR (Fig. 5C) and median rise time was 1.0 ms, 0.6–1.2 IQR (Fig. 5D). Mean halfwidth was 7.0 ± 5.0 ms (Fig. 5E). No differences were observed between uni- and birdirectional connections (Table 3). Furthermore, we found no evidence that intersomatic distance influenced connectivity rate (Fig. 5F), or any directional influence of connectivity (Fig. 5G).

Discussion

Defining the subcompartmental microcircuitry of the parahippocampal region is essential for our understanding of information flow through this circuit, as well as establishing how the spatially tuned functional properties of many of the neurons in this region arise. Here, we describe the local connectivity between the 3 major cell classes, pyramidal neurons, non-fast-spiking interneurons, and fast-spiking interneurons in the PaS, a structure that has been less well studied compared with its neighbors in the parahippocampal region.

Pyramid to Pyramid Connectivity

We observed a 4% connectivity rate between pyramidal neurons in the PaS, which is comparable to connectivity rates observed in neighboring regions containing spatially tuned neurons, including the presubiculum (4% pyramidal connectivity in deep layers; Peng et al. 2017) and the MEC (3.4% connectivity between L2/3 excitatory cells, Winterer et al. 2017). Although studies in the rat have previously divided the PaS into deep and superficial regions (Funahashi and Stewart 1997), other studies argue that the deep layers may not be associated with the PaS (Mulders et al. 1997; Burgalossi et al. 2011; Tang et al. 2016), and in the mouse this delineation is even less clear. Furthermore, although subtle differences in electrophysiological properties of the pyramidal classes are present, they lack a defined molecular basis (Sammons et al. 2019). Thus, we treated our excitatory population as one class. We did not observe any spatial influence on connectivity, neither in a nondirectional measure (intersomatic distance) nor in a directional measure (along the superficial to deep axis). This result contrasts with a previous study in the rat PaS, where a predominantly 1-way connectivity was described from superficial to deep cells (Funahashi and Stewart 1997). Moreover, this study observed strong interconnectivity between deep neurons. In contrast, we found all pairs of connected pyramidal neurons within 300 μm of the pial surface. However, it should be noted that our data are skewed to more superficially located cells due to the tapering shape of the PaS making very deep regions difficult to target. Interestingly, despite the more superficial location of our data, our results bear a striking resemblance to connectivity described in the deep layers of the presubiculum (both having 4% connectivity and within this similar levels of reciprocal connections, Peng et al. 2017) rather than the superficial layers in this region where connectivity is sparse (0.4% Peng et al. 2017). The discrepancies between our findings and those from earlier work may arise from differences in circuitry across the presubiculum and PaS, as well as species differences between rat and mouse.

Place cells in mice have lower information content and exhibit more instability than place cells in rats (Kentros et al. 2004; Hok et al. 2016). It is conceivable that such reduced stability and information content may be linked to less complex connectivity within the navigational circuitry. Moreover, the
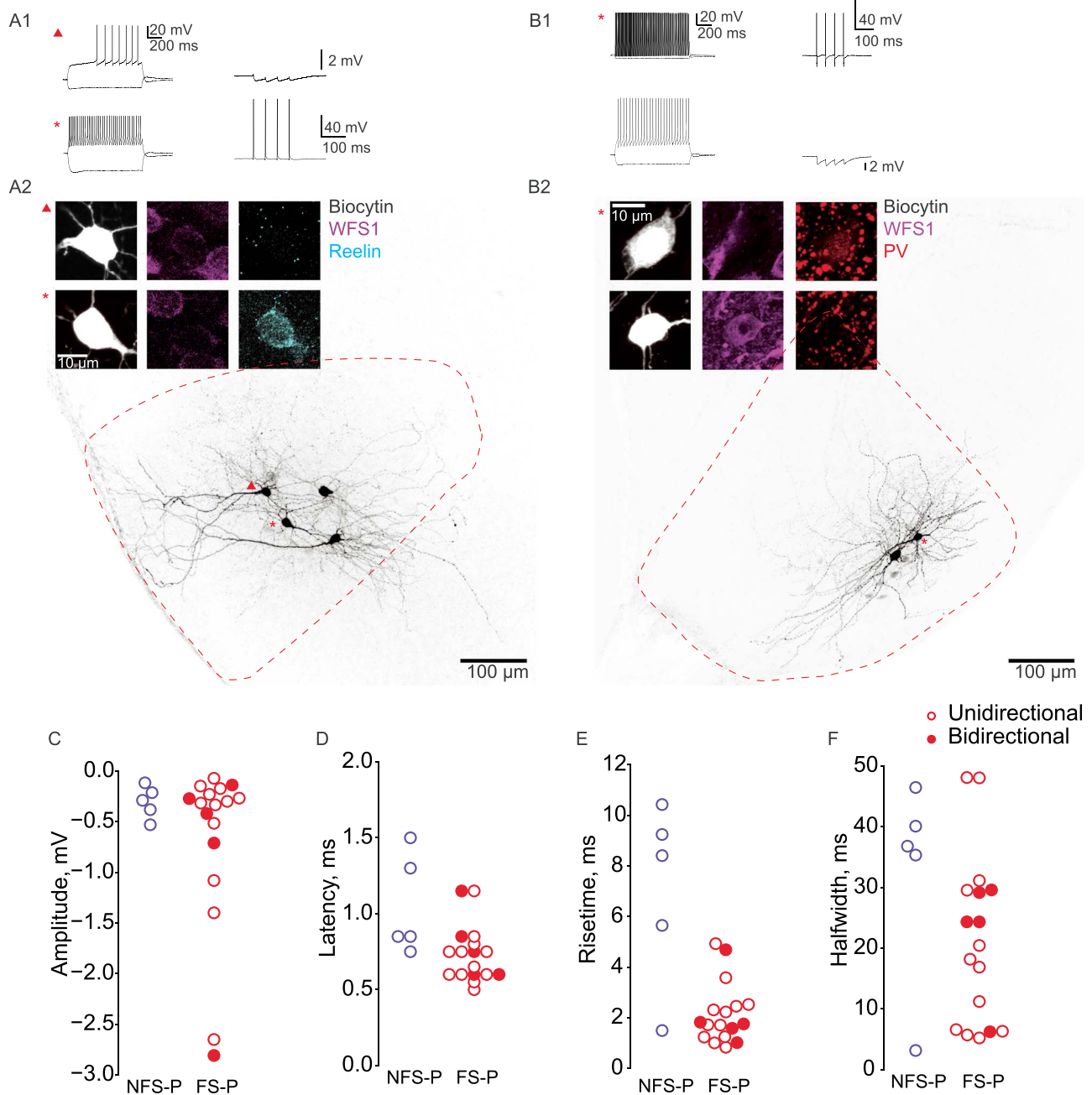
Figure 3. Inhibitory inputs onto pyramidal neurons. (A1) Left, firing profiles of a pyramidal neuron and non-fast-spiking interneuron. Right, presynaptic APs and corresponding postsynaptic response. (A2) Immunolabeling and biocytin filling of the corresponding neurons. Top row, cell is positively labeled with WFS1 but not reelin; bottom row, cell is WFS1-negative and reelin-positive. (B1) Left, firing profiles of a fast-spiking interneuron and a pyramidal neuron. Right, presynaptic APs and corresponding postsynaptic response. (B2) Immunolabeling and biocytin filling of the corresponding cells. Top row, cell is positively labeled with PV but not WFS1; bottom row, cell is WFS1-positive and PV-negative. (C) Amplitude of ISPSs from the 2 classes of interneurons onto pyramidal neurons. (D) Latency of IPSPs from the 2 interneuron classes onto pyramidal neurons. (E) Rise time of IPSPs from the 2 interneurons classes onto pyramidal neurons. (F) Halfwidth of IPSPs onto pyramidal neurons.

approach of mice and rats to navigational tasks may favor different sensory modalities, with rats more reliant on visual input and mice more heavily dependent on olfactory cues (Las and Ulanovsky 2014). Thus, given these different strategies, it is plausible that the 2 species exhibit differential routing of

information and sensory integration within the parahippocampal regions, which may ultimately be underlined by differences in wiring patterns. Therefore, our results may reflect a more condensed circuit in the mouse PaS in comparison to the rat presubiculum and PaS, where distinct patterns of connectivity
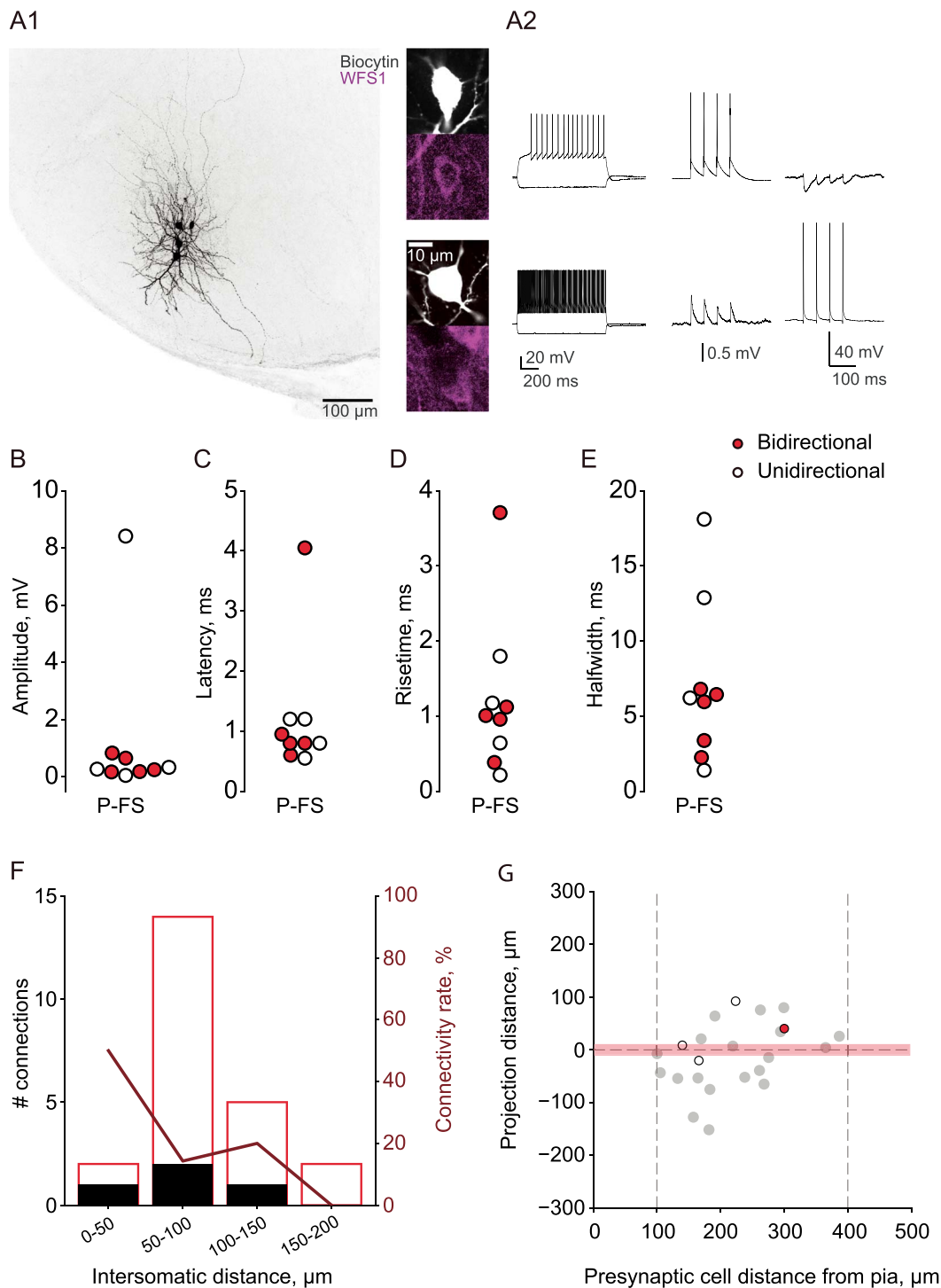
Figure 4. Spatial analysis of inhibitory to pyramidal cell connections. (A) Locations of recorded non-fast-spiking interneurons. (B) Connectivity rate between non-fast-spiking interneurons and pyramidal neurons binned by intersomatic distance. Connectivity rate does not differ significantly across distance, $P = 0.501$, ordinal association test. (C) Projection distances of tested connections from non-fast-spiking interneurons onto pyramidal neurons, with respect to presynaptic cell depth. Gray points indicate tested connections; open, blue points indicate found unidirectional connections. Deep-to-superficial: 1/7 connected; superficial-to-deep: 3/14 connected; $P = 0.999$, Fisher's exact test. (D) Locations of recorded fast-spiking interneurons. (E) Connectivity rate between fast-spiking interneurons and pyramidal neurons binned by intersomatic distance. Connectivity rate does not vary significantly across distance, $P = 0.611$, ordinal association test. (F) Projection distances between presynaptic fast-spiking interneurons and postsynaptic pyramidal neurons. Gray points indicate tested connections; open, red points indicate unidirectional connections, filled red points indicate bidirectional connections. Deep-to-superficial: 3/12 connected; superficial-to-deep: 5/8 connected; $P = 0.167$, Fisher's exact test.
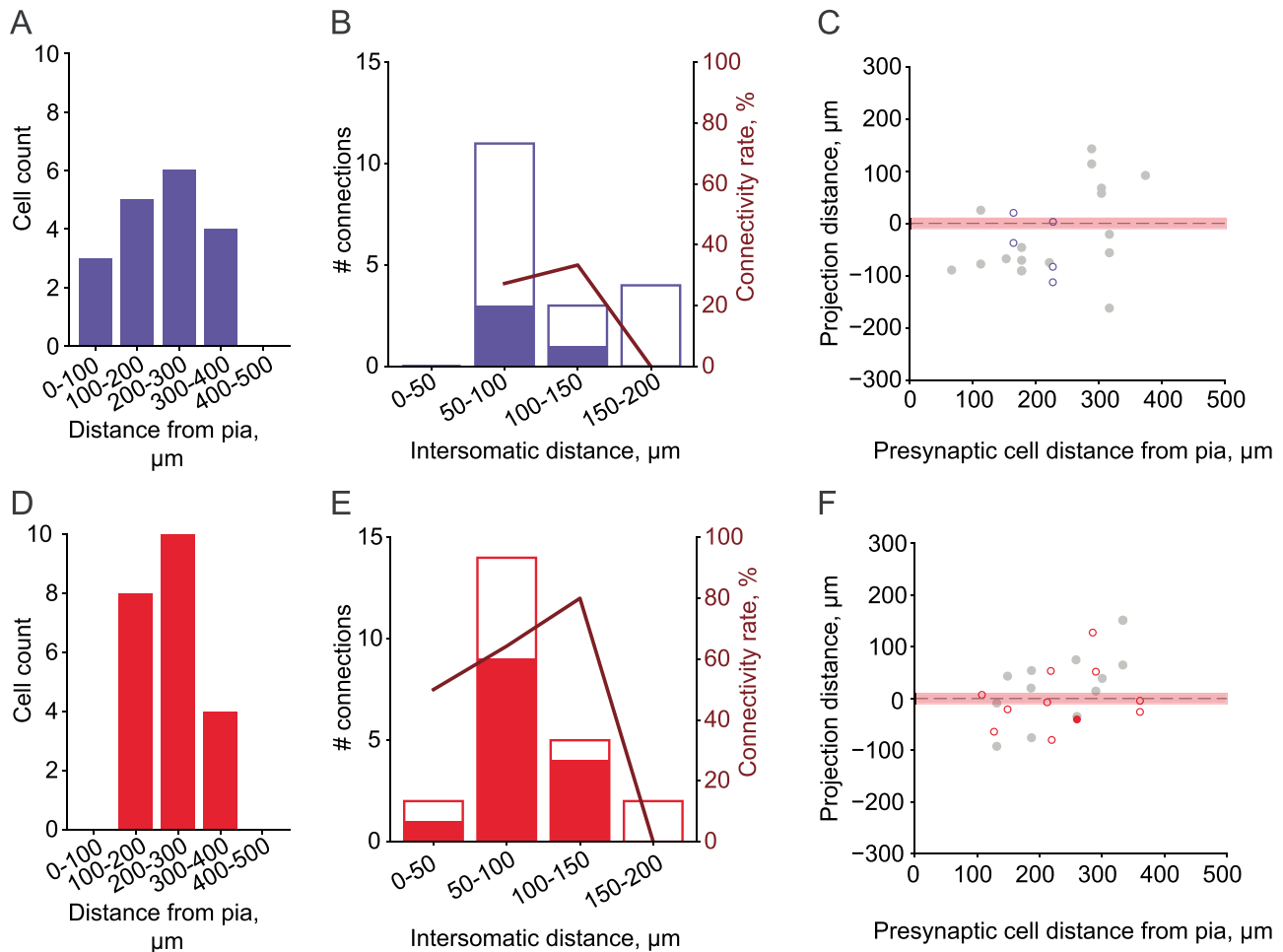
Figure 5. Connections from pyramidal neurons onto fast-spiking interneurons. (A1) Biocytin and WFS1 immunolabeling of a pyramidal cell and fast-spiking interneuron. Right, top cell is WFS1-positive, bottom cell is WFS1-negative. (A2) Left, firing profiles of pyramidal (top) and fast-spiking (bottom) neurons. Right, connectivity screen. Cells are reciprocally connected. (B) Amplitudes of EPSPs from pyramidal neurons onto fast-spiking interneurons. (C) Latency of connections from pyramidal neurons onto fast-spiking interneurons. (D) Rise time of EPSPs from pyramidal neurons onto fast-spiking neurons. (E) Halfwidth of EPSPs from pyramidal neurons onto fast-spiking interneurons. (F) Rate of connectivity across different intersomatic distances between pyramidal neurons and fast-spiking interneurons. No statistical difference was seen in connectivity rate across intersomatic distances ($P = 0.430$, ordinal association test). (G) Projection distances between pyramidal neurons onto fast-spiking interneurons. Deep-to-superficial: 2/8 connected, superficial-to-deep: 1/12 connected, $P = 0.537$, Fisher's exact test.

within and across layers are reported (Funahashi and Stewart 1997; Peng et al. 2017).

The potential lack of distance-dependence in the nondirectional measure is surprising given the several brain regions where distance-dependent connectivity has been reported, including the presubiculum (Peng et al. 2017), somatosensory cortex (Perin et al. 2011), and visual cortex (Seeman et al. 2018). This distance-dependence is thought to adhere to wiring principles aimed at balancing the economic cost of brain networks, by reducing the physical resources needed to connect synaptic partners, as well as increasing computational efficiency owing to faster conduction between neurons located closer to one another (Bullmore and Sporns 2012). The potential lack of spatial correlation in parasubicular connectivity indicates that wiring in this region may be organized by some other rules, and given the relatively small size of the PaS these may not need to be distance-regulated to maintain a wiring-cost minimization. Moreover, the observation of overrepresented reciprocal connections indicates a nonrandom nature to the connectivity in the PaS. In cortical areas, it has been shown that

cells are more likely to be connected if they share common input, functional properties or if they stem from the same progenitor cells (Yoshimura et al. 2005; Yu et al. 2009; Hofer et al. 2011; Ko et al. 2011; Cossell et al. 2015). One possibility is that grid cells, or head-direction cells with similar firing fields may be connected to one another. The functional organization of grid cells is still not fully understood. While we know that grid-scale changes across the dorsoventral axis (Hafting et al. 2005; Stensola et al. 2012), and that grid cells in the MEC physically cluster (Heys et al. 2014), we still lack a direct measurement of connectivity between grid cells within or across grid modules. Our use of acute slices precludes us from determining spatial tuning properties of the cells we record. However, advancements in imaging technology have recently enabled calcium imaging in vivo of spatially tuned cells in the MEC (Heys et al. 2014; Sun et al. 2015; Gu et al. 2018). Thus, future studies may apply a similar approach to that taken in other cortical areas and determine connectivity in acute slices between neurons previously imaged in vivo where the spatial tuning and firing fields have been discerned (Ko et al. 2011).

Pyramid and Interneuron Interactions

We classified inhibitory neurons into either non-fast-spiking or fast-spiking, using reelin and PV respectively as proxies for these 2 classes, and classifying cells based on their electrophysiological properties. Although these 2 markers alone do not cover the whole breadth of interneurons present in the PaS, together they form a large fraction of inhibitory neurons in the PaS (Sammons et al. 2019) and are known to be expressed in entirely distinct subcategories of interneurons derived from different streams of the ganglionic eminence during development (Miyoshi et al. 2010; Rudy et al. 2011). Between pyramidal neurons and non-fast-spiking interneurons, we observed a heavily skewed connectivity in favor of inhibition onto the pyramidal neurons, suggesting that the main excitatory drive onto the non-fast-spiking interneurons originates from an external source and that these neurons may provide feedforward inhibition. Although the rate of connectivity from non-fast-spiking interneurons on pyramidal cells that we observed in the PaS (13%) falls roughly in line with that in the presubiculum (9.5% in deep layers and 17.6% in superficial layers), work in the presubiculum shows similar levels of connectivity from pyramids onto non-fast-spiking interneurons (11.4% and 18.4% in deep and superficial layers, respectively) (Peng et al. 2017). This result is in stark contrast to the 2.6% connectivity we observed from pyramids onto non-fast-spiking interneurons. Thus, in the PaS there may be very low levels of feedback inhibition coming from the non-fast-spiking interneuron population compared with the presubiculum. Meanwhile, the non-fast-spiking interneurons in the PaS may play a greater role in modulating signals from other brain areas, such as the medial septum or anterior thalamus, and providing feedforward inhibition.

In contrast to the non-fast-spiking interneurons, high levels of connectivity in both directions were observed between fast-spiking interneurons and pyramidal cells (44% fast-spiking interneuron onto pyramid, 23% pyramid onto fast-spiking interneuron). Moreover, the rate of connectivity from fast-spiking interneurons onto pyramidal neurons was higher than reported in the presubiculum (10–25%; Peng et al. 2017) and fell more in line with levels of connectivity seen in cortical regions, including the MEC (Couey et al. 2013), the lateral EC (Nilssen et al. 2018) and the visual cortex (Yoshimura and Callaway 2005). Reciprocal connections were detected between fast-spiking interneurons and pyramidal neurons, and although they were not overrepresented as observed in the presubiculum (Peng et al. 2017), the high level of interconnectivity between these 2 cell classes demonstrates a feedback inhibition loop, which would provide the strong recurrent connectivity necessary for attractor network-based models of grid cell activity (Couey et al. 2013; Simonnet et al. 2017).

The strong connectivity between fast-spiking interneurons and pyramids in the PaS may also play an important role in the orchestration of theta activity in the PaS. Theta activity occurs during locomotion and exploration behaviors (Vanderwolf 1969), and during rapid eye movement (REM) sleep (Jouvet 1969). Abolishment or reduction of theta oscillations in the entorhinal cortex disrupts grid cell activity, indicating the importance of this rhythmic activity for these cells' spatial tuning (Brandon et al. 2011; Koenig et al. 2011). Moreover, the activity of an individual neuron relative to the population provides a temporal code that may be essential for spatial processing, demonstrated by phase precession. This process, whereby grid and place cells shift their firing with respect to the phase of the theta cycle as an animal traverses through the cells firing field, is thought to underlie path integration (O'Keefe and Recce 1993). Parasubicular neurons show only weak phase precession but strong rhythmic firing patterns (Glasgow and Chapman 2007; Boccara et al. 2010; Ebbesen et al. 2016; Tang et al. 2016). With their precision spike timing rendering them effective regulators of oscillatory activity (Stark et al. 2013; Amilhon et al. 2015), the fast-spiking interneurons are likely to play a key role in the maintenance of the rhythmic theta activity present in the PaS. In contrast, the presubiculum shows lower levels of theta modulation and theta-modulated grid and head-direction cells (Boccara et al. 2010; Tukker et al. 2015; Preston-Ferrer et al. 2016), which may explain the difference in interconnectivity rates between fast-spiking interneurons and pyramids across these 2 neighboring brain regions.

Log-Normal Distribution of Synaptic Weights

We observed a log-normal distribution of synaptic weights among excitatory connections, an observation that has been described in multiple brain regions including the presubiculum (Peng et al. 2017), visual cortex (Song et al. 2005; Cossell et al. 2015), somatosensory cortex (Frick et al. 2008; Lefort et al. 2009), CA3 (Ikegaya et al. 2013), CA1 (Manabe et al. 1992), and cerebellum (Isope and Barbour 2002). Moreover, log-normal distributions have been observed in numerous features in the brain from neuronal firing rates to dendritic spine sizes, and, are thought to outline a fundamental principle across different scales of brain processes (Buzsáki and Mizuseki 2014). Our finding provides further support for this general principle, and in particular, emphasizes the global nature of the phenomenon by describing log-normal synaptic weights in a brain region where they have previously not been reported. The proposed advantages for a long-tailed distribution of synaptic weights include increased network stability, optimized capacity for information storage and transmission, and a greater dynamic range for plasticity (Varshney et al. 2006; Teramae et al. 2012; Iyer et al. 2013). Strongly weighted synapses are proposed to support low frequency firing during rest periods, while the many weak synapses may maintain a neurons' membrane potential and provide a level of background noise that enhances the correlation between neurons connected by strong synapses (Teramae et al. 2012). Thus, synaptic weights in the PaS adhere to a commonly described principle of neuronal wiring.

PaS Influence on Navigational Circuitry

Our results have demonstrated that attractor-like properties exist within the PaS, and thus, according to models, the connectivity within this brain region would be capable of supporting grid cell firing patterns. The mechanisms generating grid cell firing, in particular in layer 2 of the MEC where the majority of grid cells are found (Boccara et al. 2010), remain unclear. Computational models have predicted both recurrent connectivity and theta oscillations as essential features for the emergence of spatial firing (Fuhs and Touretzky 2006; McNaughton et al. 2006; Hasselmo et al. 2007; Burak and Fiete 2009; Brandon et al. 2011; Burgess and O'Keefe 2011). Here, we demonstrate connections that may represent both of these features and, provide additional information and constraints for the further development of such models. The observed interpyramidal connectivity, along with the frequent interactions between

pyramidal cells and fast-spiking interneurons fit attractor network properties for supporting spatially tuned firing. Moreover, the strong interactions between pyramidal cells and fast-spiking interneurons may orchestrate theta rhythmicity in the PaS and maintain subthreshold oscillations in the membrane potential of pyramidal neurons.

Upon repeated exposure to environments, grid cells and head direction cells maintain similar phase and orientation preferences with reference to external cues (Hafting et al. 2005), indicating that sensory inputs including visual and vestibular information may be crucial. The PaS, along with the presubiculum, is one of the first regions in the circuitry showing grid cell activity. Therefore, incoming projections from regions including the anterior thalamus, with head-direction information, combined with the local connectivity demonstrated here may suffice to generate grid cell-like firing patterns. Non-fast-spiking interneurons in the PaS may be involved in the modulation of the incoming projections via feedforward inhibition, whereas fast-spiking interneurons may orchestrate the temporal integration of signals.

Combined with previous anatomical work demonstrating the strong connection between PaS and the MEC, the PaS may be a source of grid cell activity from which the MEC can inherit and refine these tuning properties. The spatial firing generated in the PaS may be carried downstream to the region's major output target, the MEC. This information may be directly transmitted to layer 2 principal cells, the most populous site of grid cells. Alternatively, the information may reach layer 2 indirectly via connections to other layers including layer 3 (Canto et al. 2012), which in turn drives layer 2 stellate cells (Winterer et al. 2017). Future studies may address the cell-type specificity of PaS connections to the MEC. All in all, our findings on the electrophysiological and connectivity profiles of the PaS neurons can be used to further develop detailed single cell and network level biophysical plausible models of the PaS. Future modeling work would potentially investigate how the intrinsic cellular properties and the network level motifs between the excitatory and inhibitory PaS populations may serve the generation of grid-like behavior and the overall computations in this area.

Summary

In summary, we find that the microcircuitry of the PaS shares some common features with local circuits in other parahippocampal regions. Specifically, levels of excitatory connectivity were similar to the presubiculum and MEC, and the nonrandom organization was further reminiscent of the presubiculum. Interactions between pyramidal neurons and fast-spiking interneurons were strong, similar to many cortical regions, and likely play an important role in the temporal organization of activity in this region. We observed overrepresentation of reciprocally connected pyramids, indicating nonrandom organization of connectivity. However, in contrast to reports from numerous brain regions, we did not observe distance dependence of connectivity. Thus, our work supports the notion that local wiring circuits in the brain follow a number of fundamental principles (nonrandom, log-normal synaptic weights), whereas region-specific divergences (levels of inhibition, distance-wiring rules) may allow for function-specific processing. Moreover, our work complements the growing field of connectomics, and more specifically fills a gap in our current knowledge of the navigational circuitry by elucidating the connectivity scheme within the PaS.

Supplementary Material

Supplementary material can be found at *Cerebral Cortex* online.

Funding

Notes

References

Agster KL, Burwell RD. 2013. Hippocampal and subicular efferents and afferents of the perirhinal, postrhinal, and entorhinal cortices of the rat. *Behav Brain Res*. 254:50–64.

Amilhon B, Huh CYL, Manseau F, Ducharme G, Nichol H, Adamantidis A, Williams S. 2015. Parvalbumin interneurons of hippocampus tune population activity at theta frequency. *Neuron*. 86:1277–1289.

Blackstad TW. 1956. Commissural connections of the hippocampal region in the rat, with special reference to their mode of termination. *J Comp Neurol*. 105:417–537.

Blair HT, Gupta K, Zhang K. 2008. Conversion of a phase- to a rate-coded position signal by a three-stage model of theta cells, grid cells, and place cells. *Hippocampus*. 18:1239–1255.

Boccara CN, Sargolini F, Thoresen VH, Solstad T, Witter MP, Moser EI, Moser M-B. 2010. Grid cells in pre- and parasubiculum. *Nat Neurosci*. 13:987–994.

Brandon MP, Bogaard AR, Libby CP, Connerney MA, Gupta K, Hasselmo ME. 2011. Reduction of theta rhythm dissociates grid cell spatial periodicity from directional tuning. *Science*. 332:595–599.

Buetfering C, Allen K, Monyer H. 2014. Parvalbumin interneurons provide grid cell-driven recurrent inhibition in the medial entorhinal cortex. *Nat Neurosci*. 17:710–718.

Bullmore E, Sporns O. 2012. The economy of brain network organization. *Nat Rev Neurosci*. 13:336–349.

Burak Y, Fiete IR. 2009. Accurate path integration in continuous attractor network models of grid cells. *PLoS Comput Biol*. 5:e1000291.

Burgalossi A, Herfst L, von Heimendahl M, Förste H, Haskic K, Schmidt M, Brecht M. 2011. Microcircuits of functionally identified neurons in the rat medial entorhinal cortex. *Neuron*. 70:773–786.

Burgess N, O'Keefe J. 2011. Models of place and grid cell firing and theta rhythmicity. *Curr Opin Neurobiol*. 21:734–744.

Burgess N, Barry C, O'Keefe J. 2007. An oscillatory interference model of grid cell firing. *Hippocampus*. 17:801–812.

Bush D, Burgess N. 2014. A hybrid oscillatory interference/continuous attractor network model of grid cell firing. *J Neurosci*. 34:5065–79.

Buzsáki G. 2002. Theta oscillations in the hippocampus. *Neuron*. 33:325–340.

Buzsáki G, Mizuseki K. 2014. The log-dynamic brain: how skewed distributions affect network operations. *Nat Rev Neurosci*. 15:264–278.

Caballero-Bleda M, Witter MP. 1993. Regional and laminar organization of projections from the presubiculum and parasubiculum to the entorhinal cortex: an anterograde tracing study in the rat. *J Comp Neurol*. 328:115–129.

Cacucci F, Lever C, Wills TJ, Burgess N, O'Keefe J. 2004. Theta-modulated place-by-direction cells in the hippocampal formation in the rat. *J Neurosci*. 24:8265–8277.

Canto CB, Koganezawa N, Beed P, Moser EI, Witter MP. 2012. All layers of medial entorhinal cortex receive presubicular and parasubicular inputs. *J Neurosci*. 32:17620–17631.

Cossell L, Iacaruso MF, Muir DR, Houlton R, Sader EN, Ko H, Hofer SB, Mrsic-Flogel TD. 2015. Functional organization of excitatory synaptic strength in primary visual cortex. *Nature*. 518:399–403.

Couey JJ, Witoelar A, Zhang S-J, Zheng K, Ye J, Dunn B, Czajkowski R, Moser M-B, Moser EI, Roudi Y, et al. 2013. Recurrent inhibitory circuitry as a mechanism for grid formation. *Nat Neurosci*. 16:318–324.

Ding S-L. 2013. Comparative anatomy of the prosubiculum, subiculum, presubiculum, postsubiculum, and parasubiculum in human, monkey, and rodent. *J Comp Neurol*. 521:4145–4162.

Ebbesen CL, Reifenstein ET, Tang Q, Burgalossi A, Ray S, Schreiber S, Kempter R, Brecht M. 2016. Cell type-specific differences in spike timing and spike shape in the rat parasubiculum and superficial medial entorhinal cortex. *Cell Rep*. 16:1005–1015.

Frick A, Feldmeyer D, Helmstaedter M, Sakmann B. 2008. Monosynaptic connections between Pairs of L5A pyramidal neurons in columns of juvenile rat somatosensory cortex. *Cereb Cortex*. 18:397–406.

Fuchs EC, Neitz A, Pinna R, Melzer S, Caputi A, Monyer H. 2016. Local and distant input controlling excitation in layer II of the medial entorhinal cortex. *Neuron*. 89:194–208.

Fuhs MC, Touretzky DS. 2006. A spin glass model of path integration in rat medial entorhinal cortex. *J Neurosci*. 26:4266–4276.

Fujimaru Y, Kosaka T. 1996. The distribution of two calcium binding proteins, calbindin D-28K and parvalbumin, in the entorhinal cortex of the adult mouse. *Neurosci Res*. 24:329–343.

Funahashi M, Stewart M. 1997. Presubicular and parasubicular cortical neurons of the rat: functional separation of deep and superficial neurons in vitro. *J Physiol*. 501(Pt 2):387–403.

Funahashi M, Stewart M. 1998. GABA receptor-mediated postsynaptic potentials in the retrohippocampal cortices: regional, laminar and cellular comparisons. *Brain Res*. 787:19–33.

Glasgow SD, Chapman CA. 2007. Local generation of theta-frequency EEG activity in the parasubiculum. *J Neurophysiol*. 97:3868–3879.

Glasgow SD, Chapman CA. 2008. Conductances mediating intrinsic theta-frequency membrane potential oscillations in layer II parasubicular neurons. *J Neurophysiol*. 100:2746–2756.

van Groen T, Wyss JM. 1990. The connections of presubiculum and parasubiculum in the rat. *Brain Res*. 518:227–243.

Gu Y, Lewallen S, Kinkhabwala AA, Domnisoru C, Yoon K, Gauthier JL, Fiete IR, Tank DW. 2018. A map-like microorganization of grid cells in the medial entorhinal cortex. *Cell*. 175:736–750.e30.

Guzman SJ, Schlögl A, Schmidt-Hieber C. 2014. Stimfit: quantifying electrophysiological data with python. *Front Neuroinform*. 8:16.

Hafting T, Fyhn M, Molden S, Moser M-B, Moser EI. 2005. Microstructure of a spatial map in the entorhinal cortex. *Nature*. 436:801–806.

Hasselmo ME, Brandon MP. 2012. A model combining oscillations and attractor dynamics for generation of grid cell firing. *Front Neural Circuits*. 6:30.

Hasselmo ME, Giocomo LM, Zilli EA. 2007. Grid cell firing may arise from interference of theta frequency membrane potential oscillations in single neurons. *Hippocampus*. 17:1252–1271.

Heys JG, Rangarajan KV, Dombeck DA. 2014. The functional micro-organization of grid cells revealed by cellular-resolution imaging. *Neuron*. 84:1079–1090.

Hofer SB, Ko H, Pichler B, Vogelstein J, Ros H, Zeng H, Lein E, Lesica NA, Mrsic-Flogel TD. 2011. Differential connectivity and response dynamics of excitatory and inhibitory neurons in visual cortex. *Nat Neurosci*. 14:1045–1052.

Hok V, Poucet B, Duvelle É, Save É, Sargolini F. 2016. Spatial cognition in mice and rats: similarities and differences in brain and behavior. *WIREs Cogn Sci*. 7:406–421.

Ikegaya Y, Sasaki T, Ishikawa D, Honma N, Tao K, Takahashi N, Minamisawa G, Ujita S, Matsuki N. 2013. Interpyramid spike transmission stabilizes the sparseness of recurrent network activity. *Cereb Cortex*. 23:293–304.

Isope P, Barbour B. 2002. Properties of unitary granule cell→purkinje cell synapses in adult rat cerebellar slices. *J Neurosci*. 22:9668–9678.

Iyer R, Menon V, Buice M, Koch C, Mihalas S. 2013. The influence of synaptic weight distribution on neuronal population dynamics. *PLoS Comput Biol*. 9:e1003248.

Jouvet M. 1969. Biogenic amines and the states of sleep. *Science*. 163:32–41.

Kentros CG, Agnihotri NT, Streater S, Hawkins RD, Kandel ER. 2004. Increased attention to spatial context increases both place field stability and spatial memory. *Neuron*. 42:283–295.

Kitamura T, Pignatelli M, Suh J, Kohara K, Yoshiki A, Abe K, Tonegawa S. 2014. Island cells control temporal association memory. *Science*. 343:896–901.

Ko H, Hofer SB, Pichler B, Buchanan KA, Sjöström PJ, Mrsic-Flogel TD. 2011. Functional specificity of local synaptic connections in neocortical networks. *Nature*. 473:87–91.

Koenig J, Linder AN, Leutgeb JK, Leutgeb S. 2011. The spatial periodicity of grid cells is not sustained during reduced theta oscillations. *Science*. 332:592–595.

Köhler C. 1986. Intrinsic connections of the retrohippocampal region in the rat brain. II. The medial entorhinal area. *J Comp Neurol*. 246:149–169.

Las L, Ulanovsky N. 2014. Hippocampal neurophysiology across species. In: Derdikman D, Knierim JJ, editors. *Space, Time and Memory in the Hippocampal Formation*. Vienna: Springer, pp. 431–461.

Lefort S, Tomm C, Floyd Sarria J-C, Petersen CCH. 2009. The excitatory neuronal network of the C2 barrel column in mouse primary somatosensory cortex. *Neuron.* 61:301–316.

Liu P, Jarrard LE, Bilkey DK. 2001. Excitotoxic lesions of the pre- and parasubiculum disrupt object recognition and spatial memory processes. *Behav Neurosci.* 115:112–124.

Liu P, Jarrard LE, Bilkey DK. 2004. Excitotoxic lesions of the pre- and parasubiculum disrupt the place fields of hippocampal pyramidal cells. *Hippocampus.* 14:107–116.

Luuk H, Koks S, Plaas M, Hannibal J, Rehfeld JF, Vasar E. 2008. Distribution of Wfs1 protein in the central nervous system of the mouse and its relation to clinical symptoms of the Wolfram syndrome. *J Comp Neurol.* 509:642–660.

Manabe T, Renner P, Nicoll RA. 1992. Postsynaptic contribution to long-term potentiation revealed by the analysis of miniature synaptic currents. *Nature.* 355:50–55.

McNaughton BL, Battaglia FP, Jensen O, Moser EI, Moser M-B. 2006. Path integration and the neural basis of the cognitive map. *Nat Rev Neurosci.* 7:663–678.

Mitchell SJ, Rawlins JN, Steward O, Olton DS. 1982. Medial septal area lesions disrupt theta rhythm and cholinergic staining in medial entorhinal cortex and produce impaired radial arm maze behavior in rats. *J Neurosci.* 2:292–302.

Miyoshi G, Hjerling-Leffler J, Karayannis T, Sousa VH, Butt SJB, Battiste J, Johnson JE, Machold RP, Fishell G. 2010. Genetic fate mapping reveals that the caudal ganglionic eminence produces a large and diverse population of superficial cortical interneurons. *J Neurosci.* 30:1582–1594.

Moser EI, Kropff E, Moser M-B. 2008. Place cells, grid cells, and the brain's spatial representation system. *Annu Rev Neurosci.* 31:69–89.

Mulders WH, West MJ, Slomianka L. 1997. Neuron numbers in the presubiculum, parasubiculum, and entorhinal area of the rat. *J Comp Neurol.* 385:83–94.

Nilssen ES, Jacobsen B, Fjeld G, Nair RR, Blankvoort S, Kentros C, Witter MP. 2018. Inhibitory connectivity dominates the fan cell network in layer II of lateral entorhinal cortex. *J Neurosci.* 38:9712–9727.

O'Keefe J, Dostrovsky J. 1971. The hippocampus as a spatial map. Preliminary evidence from unit activity in the freely-moving rat. *Brain Res.* 34:171–175.

O'Keefe J, Recce ML. 1993. Phase relationship between hippocampal place units and the EEG theta rhythm. *Hippocampus.* 3:317–330.

O'Reilly KC, Gulden Dahl A, Ulsaker Kruge I, Witter MP. 2013. Subicular-parahippocampal projections revisited: Development of a complex topography in the rat: developing subicular-parahippocampal projections. *J Comp Neurol.* 521:4284–4299.

Peng Y, Barreda Tomás FJ, Klisch C, Vida I, Geiger JRP. 2017. Layer-specific organization of local excitatory and inhibitory synaptic connectivity in the rat presubiculum. *Cereb Cortex N Y N. 1991*(27):2435–2452.

Perin R, Berger TK, Markram H. 2011. A synaptic organizing principle for cortical neuronal groups. *Proc Natl Acad Sci.* 108:5419–5424.

Petsche H, Stumpf C, Gogolak G. 1962. The significance of the rabbit's septum as a relay station between the midbrain and the hippocampus I. The control of hippocampus arousal activity by the septum cells. *Electroencephalogr Clin Neurophysiol.* 14:202–211.

Preston-Ferrer P, Coletta S, Frey M, Burgalossi A. 2016. Anatomical organization of presubicular head-direction circuits. *elife.* 5:e14592.

Ramsden HL, Sürmeli G, McDonagh SG, Nolan MF. 2015. Laminar and Dorsoventral Molecular Organization of the Medial Entorhinal Cortex revealed by large-scale anatomical analysis of gene expression. *PLoS Comput Biol.* 11:e1004032.

Ray S, Brecht M. 2016. Structural development and dorsoventral maturation of the medial entorhinal cortex. *elife.* 5:e13343.

Ray S, Burgalossi A, Brecht M, Naumann RK. 2017. Complementary modular microcircuits of the rat medial entorhinal cortex. *Front Syst Neurosci.* 11:20.

Rudy B, Fishell G, Lee S, Hjerling-Leffler J. 2011. Three groups of interneurons account for nearly 100% of neocortical GABAergic neurons. *Dev Neurobiol.* 71:45–61.

Sammons RP, Parthier D, Stumpf A, Schmitz D. 2019. Electrophysiological and molecular characterization of the parasubiculum. *J Neurosci.* 39:8860–8876.

Schindelin J, Arganda-Carreras I, Frise E, Kaynig V, Longair M, Pietzsch T, Preibisch S, Rueden C, Saalfeld S, Schmid B, et al. 2012. Fiji: an open-source platform for biological-image analysis. *Nat Methods.* 9:676–682.

Schmidt-Hieber C, Häusser M. 2013. Cellular mechanisms of spatial navigation in the medial entorhinal cortex. *Nat Neurosci.* 16:325–331.

Seeman SC, Campagnola L, Davoudian PA, Hoggarth A, Hage TA, Bosma-Moody A, Baker CA, Lee JH, Mihalas S, Teeter C, et al. 2018. Sparse recurrent excitatory connectivity in the microcircuit of the adult mouse and human cortex. *elife.* 7:e37349.

Simonnet J, Nassar M, Stella F, Cohen I, Mathon B, Boccara CN, Miles R, Fricker D. 2017. Activity dependent feedback inhibition may maintain head direction signals in mouse presubiculum. *Nat Commun.* 8:16032.

Slomianka L, Geneser FA. 1991. Distribution of acetylcholinesterase in the hippocampal region of the mouse: I. Entorhinal area, parasubiculum, retrosplenial area, and Presubiculum. *J Comp Neurol.* 303:339–354.

Song S, Sjöström PJ, Reigl M, Nelson S, Chklovskii DB. 2005. Highly nonrandom features of synaptic connectivity in local cortical circuits. *PLoS Biol.* 3:e68.

Stark E, Eichler R, Roux L, Fujisawa S, Rotstein HG, Buzsáki G. 2013. Inhibition-induced theta resonance in cortical circuits. *Neuron.* 80.

Stensola H, Stensola T, Solstad T, Frøland K, Moser M-B, Moser EI. 2012. The entorhinal grid map is discretized. *Nature.* 492:72–78.

Sun C, Kitamura T, Yamamoto J, Martin J, Pignatelli M, Kitch LJ, Schnitzer MJ, Tonegawa S. 2015. Distinct speed dependence of entorhinal island and ocean cells, including respective grid cells. *Proc Natl Acad Sci U S A.* 112:9466–9471.

Tang Q, Burgalossi A, Ebbesen CL, Sanguinetti-Scheck JI, Schmidt H, Tukker JJ, Naumann R, Ray S, Preston-Ferrer P, Schmitz D, et al. 2016. Functional architecture of the rat parasubiculum. *J Neurosci.* 36:2289–2301.

Taube JS. 2007. The head direction signal: origins and sensorymotor integration. *Annu Rev Neurosci.* 30:181–207.

Taube JS, Muller RU, Ranck JB. 1990. Head-direction cells recorded from the postsubiculum in freely moving rats. I. Description and quantitative analysis. *J Neurosci.* 10:420–435.

Teramae J, Tsubo Y, Fukai T. 2012. Optimal spike-based communication in excitable networks with strong-sparse and weak-dense links. *Sci Rep*. 2:485.

Tsanov M, Chah E, Vann SD, Reilly RB, Erichsen JT, Aggleton JP, O'Mara SM. 2011. Theta-modulated head direction cells in the rat anterior thalamus. *J Neurosci*. 31:9489–9502.

Tukker JJ, Tang Q, Burgalossi A, Brecht M. 2015. Head-directional tuning and theta modulation of anatomically identified neurons in the presubiculum. *J Neurosci*. 35:15391–15395.

Unal G, Joshi A, Viney TJ, Kis V, Somogyi P. 2015. Synaptic targets of medial septal projections in the hippocampus and extrahippocampal cortices of the mouse. *J Neurosci*. 35:15812–15826.

Vanderwolf CH. 1969. Hippocampal electrical activity and voluntary movement in the rat. *Electroencephalogr Clin Neurophysiol*. 26:407–418.

Varga C, Lee SY, Soltesz I. 2010. Target-selective GABAergic control of entorhinal cortex output. *Nat Neurosci*. 13:822–824.

Varshney LR, Sjöström PJ, Chklovskii DB. 2006. Optimal information storage in noisy synapses under resource constraints. *Neuron*. 52:409–423.

Winter SS, Clark BJ, Taube JS. 2015. Spatial navigation. Disruption of the head direction cell network impairs the parahippocampal grid cell signal. *Science*. 347: 870–874.

Winterer J, Maier N, Wozny C, Beed P, Breustedt J, Evangelista R, Peng Y, D'Albis T, Kempter R, Schmitz D. 2017. Excitatory microcircuits within superficial layers of the medial entorhinal cortex. *Cell Rep*. 19:1110–1116.

Witter MP, Doan TP, Jacobsen B, Nilssen ES, Ohara S. 2017. Architecture of the entorhinal cortex a review of entorhinal anatomy in rodents with some comparative notes. *Front Syst Neurosci*. 11:46.

Yoshimura Y, Callaway EM. 2005. Fine-scale specificity of cortical networks depends on inhibitory cell type and connectivity. *Nat Neurosci*. 8:1552–1559.

Yoshimura Y, Dantzker JLM, Callaway EM. 2005. Excitatory cortical neurons form fine-scale functional networks. *Nature*. 433:868–873.

Yu Y-C, Bultje RS, Wang X, Shi S-H. 2009. Specific synapses develop preferentially among sister excitatory neurons in the neocortex. *Nature*. 458:501–504.